

Real-time optical characterization of surface acoustic modes of polyimide thin-film coatings

Anil R. Duggal, John A. Rogers, and Keith A. Nelson

Department of Chemistry, Massachusetts Institute of Technology, Cambridge, Massachusetts 02139

(Received 27 December 1991; accepted for publication 2 June 1992)

A modification of the optical technique of impulsive stimulated thermal scattering that allows real-time data acquisition is introduced. The method is used to characterize the pseudo-Rayleigh acoustic modes of thin ($\sim 1 \mu\text{m}$) polyimide films attached to silicon substrates and its potential use as a means for extracting the elastic constants of thin-film coatings is demonstrated.

I. INTRODUCTION

Characterization of acoustic and thermal properties of thin ($\sim 1 \mu\text{m}$) polymeric films either free standing or used as coatings is of great technological importance for the polymer, microelectronics, and biomedical industries. The ideal method for doing this would be noninvasive and would be applicable to films in their final configurations or during fabrication and curing. A rapid, noninvasive characterization method could be used for feedback and control over thin-film fabrication and curing.

Impulsive stimulated thermal scattering (ISTS) is a time-resolved optical spectroscopy method that has been used extensively for characterization of bulk samples.^{1,2} In ISTS, absorption of crossed picosecond excitation pulses in a sample gives rise to spatially periodic heating and thermal expansion which launches counterpropagating acoustic waves. The acoustic oscillations and decay, and finally thermal diffusion, are monitored through measurement of the time-dependent diffraction of a third probe beam. ISTS has been used for the determination of elastic constants and thermal diffusion rates in bulk samples.³ ISTS has previously been applied to probe the acoustic responses of samples on the order of micrometer thickness by Meth, Marshall, and Fayer⁴ for thin flakes of naphthalene and by Rao *et al.*⁵ for thin polystyrene layers doped with naphthalene to induce optical absorption. In the earlier bulk and thin-film studies, data acquisition involved many repetitions (typically thousands) of an excitation-probe pulse sequence as described below. This leads to long data collection times and in some cases to cumulative sample heating and damage. In a previous study of a polymer film⁵ the sample was translated during data collection to avoid excessive heating and damage. Such a scheme is not feasible when data is collected in reflection mode (for opaque samples as described below) since slight sample warping leads to movement of the signal beam upon translation. In a recent preliminary report,⁶ we described a modification of the ISTS technique that allows real-time characterization of the acoustic modes of thin supported films. Data can be collected with minimal signal averaging and even a single excitation-probe pulse sequence can yield adequate signal.

In this paper, we describe these modifications in more detail and demonstrate the utility of the technique in analyzing the pseudo-Rayleigh or Sezawa acoustic waves propagating on a thin polyimide film attached to a silicon

substrate. We also present a detailed analysis of these modes. The main purpose of the treatment is to determine which modes are excited most effectively by the crossed excitation pulses and which contribute most to the diffraction of probe light. It will be shown that this determination can simplify the extraction of the elastic properties of the system from ISTS data.

We note that Brillouin scattering offers an alternative optical method for the characterization of thin-film acoustic modes.⁷ However, extensive practical applications are unlikely at present since data acquisition times for these studies range from 20–30 h.

II. THE ISTS EXPERIMENT ON THIN SUPPORTED FILMS

In ISTS, two ultrashort excitation pulses are crossed temporally and spatially at the sample. An optical interference pattern characterized by scattering wave vector \mathbf{q} is formed, where \mathbf{q} is the difference between the wave vectors of the crossed pulses. Optical absorption followed by rapid nonradiative relaxation leads to the sudden formation of a temperature grating which images the optical interference pattern. Thermal expansion results in the launching of counterpropagating acoustic waves as well as a steady-state density modulation which persists until thermal diffusion returns the system to equilibrium. The time-dependent material response is probed by monitoring the extent of diffraction of probe laser light off the density grating. In ISTS experiments to date, a picosecond probe pulse has been used to determine the diffracted signal intensity at a particular time following excitation of the sample. The time dependence of the response is obtained by repeating the excitation-probe pulse sequence with different delays of the probe relative to the pump pulse. Data collection times (with laser repetition rates of about 1 kHz) are typically at least several minutes for short scans with strong signal levels, and can be several hours for long scans or very weak signals.

The modification of the ISTS technique described here involves use of a cw probe laser beam or a probe laser pulse whose duration is long compared to that of the material response of interest. The time dependence of the material response is then obtained by electronically analyzing the time dependence of the diffracted probe beam. In contrast to traditional ISTS, this allows the entire response to be

III. EXPERIMENT

The polyimide/Si samples were made by spin coating and then fully curing Dupont Pyralin 2555 onto 330- μm -thick silicon wafers. The polyimide films used in this study were 0.92, 1.97, 2.04, 4.01, 4.29, and 5.81 μm thick as measured using a mechanical stylus profilometer and are accurate to within $\pm 0.05 \mu\text{m}$. In addition, a 5.99 μm polyimide layer was spin coated onto a quartz substrate so that the polyimide absorption spectrum could be measured with a standard transmissive UV-visible spectrophotometer.

The ISTS experimental setup is shown schematically in Fig. 1. The excitation pulse is derived from the output of a Q-switched, mode-locked, and cavity-dumped Nd:YAG laser which yields a 1 mJ 1064 nm pulse of 100 ps duration at a repetition rate of up to 1 kHz. This light is first attenuated and then passed through a lithium triborate (LBO) crystal to yield light at 532 nm. This is then mixed with the remnant 1064 nm radiation in a β -barium borate (BBO) crystal to yield excitation pulses of approximately 10 μJ at 355 nm. This wavelength matches the red edge of the polyimide electronic absorption spectrum and leads to efficient heating. As shown in Fig. 1, the pulse is split with a 50% reflector to yield the two excitation pulses that are crossed at an excitation angle θ at the film surface. The probe beam is derived from a second Q-switched Nd:YAG laser running at the same repetition rate as the excitation laser. The output is frequency doubled in a second BBO crystal to yield a 532 nm probe pulse of approximately 300 ns duration (see inset of Fig. 2). The probe pulse is overlapped

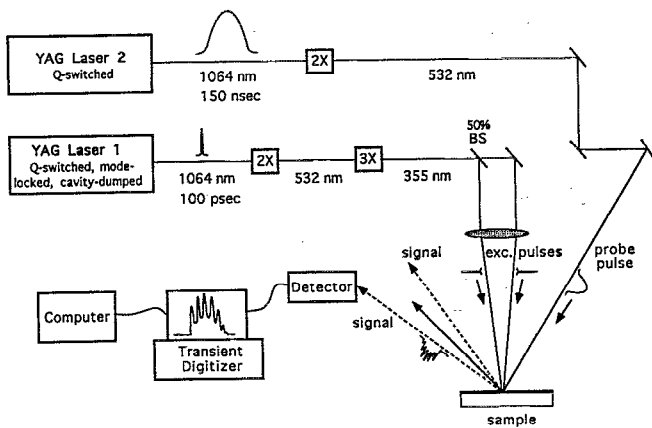


FIG. 1. Experimental setup for real-time ISTS experiments on thin-film coatings. Two picosecond excitation pulses at 355 nm are crossed at the sample surface. The “quasi-cw” probe pulse at 532 nm is spatially and temporally overlapped with the excitation beams at the sample and the diffracted signal is time resolved electronically with a transient digitizer. BS: beamsplitter; 2 \times , 3 \times : second- and third-harmonic generators.

analyzed with each excitation-probe pulse sequence. With current high-speed electronic capabilities, it is thus possible to characterize acoustic excitations with oscillation frequencies of up to 1 GHz in real time. This modification has made possible routine ISTS analysis of polymer films. Using conventional methods, optical damage to the film could not be avoided.

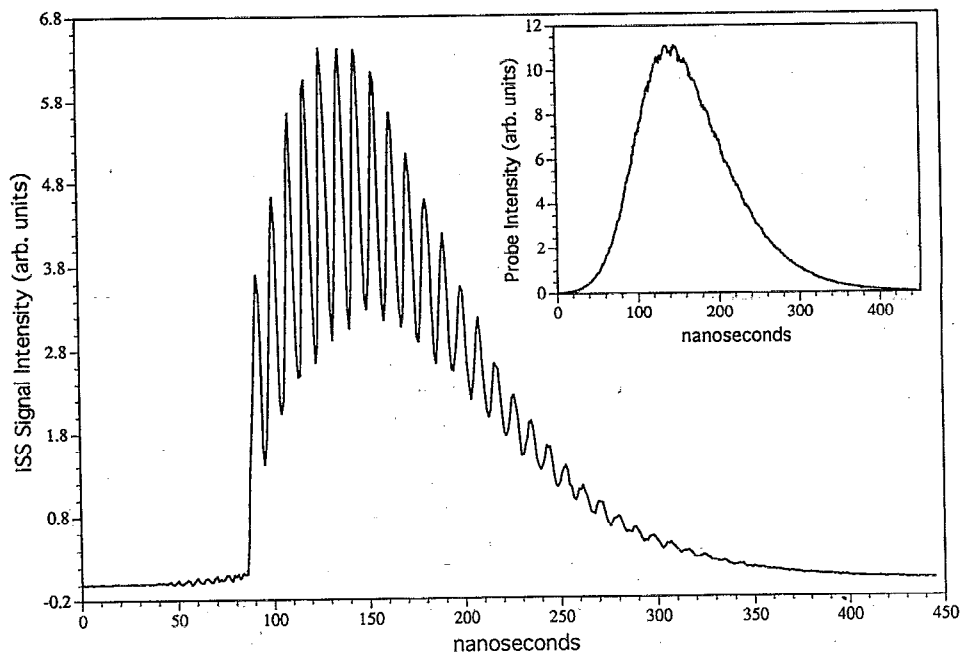


FIG. 2. Diffracted ISTS signal from a 5.81 μm Dupont Pyralin 2555 film on a silicon substrate with acoustic wave vector $0.28 \mu\text{m}^{-1}$. The signal is the result of averaging over 500 pump-probe laser pulse sequences. The inset shows the temporal profile of the Q-switched probe pulse, also averaged over 500 pulses.

spatially and temporally with the excitation pulses at the film surface.

Since the silicon substrate is opaque to the probe radiation, the experiments were performed in a reflection geometry as depicted in Fig. 1. For these thin samples, the Bragg diffraction condition is relaxed and diffraction occurs for any probe angle of incidence. However, as will be discussed later there can be a complicated angular dependence for diffraction efficiency from thin-film gratings. In these studies the probe beam was kept at a fixed angle of approximately 45°. One of the two diffracted signal beams was detected using a fast amplified photodiode (Antel Co., 2 GHz bandwidth) and then time resolved with a transient digitizer (Tektronix DSA 602, 1 GHz bandwidth). This digitized signal was then transferred to a computer for subsequent analysis. The laser repetition rate used for these experiments was only 100 Hz since faster rates could not be utilized by the transient digitizer. We note that a cw probe beam may also be used, and this has been done recently for bulk samples which give strong ISTS signals.⁸ However, we were unable to find the weaker signals from thin films using an electronically gated argon-ion probe laser. The *Q*-switched probe pulse is advantageous because its intensity is about 50 times higher, and there is no background cw light that can contribute to noise and sample damage.

Data were recorded as a function of the excitation angle θ for all the polyimide/Si sample thicknesses. The scattering wave-vector magnitude q associated with each excitation angle can be calculated according to

$$q = \frac{4\pi \sin(\theta/2)}{\lambda}, \quad (1)$$

where λ is the wavelength of the excitation light. The angles used in this study were 0.48°, 0.68°, 0.72°, 0.92°, 1.07°, 1.17°, 1.62°, 1.67°, 1.77°, 1.93°, 2.37°, 3.40°, 3.92°, and 5.85°. These angles were measured mechanically using a calibrated rotation stage and are accurate to $\pm 0.05^\circ$. The corresponding scattering wave vectors according to Eq. (1) are 0.15, 0.21, 0.22, 0.28, 0.33, 0.36, 0.50, 0.52, 0.55, 0.60, 0.73, 1.05, 1.21, and 1.81 μm^{-1} . These are accurate to $\pm 0.01 \mu\text{m}^{-1}$. The wave vectors were chosen to lie along a crystal axis of the silicon substrate. However, experiments performed with a wave-vector magnitude of 0.52 μm^{-1} on the 5.81 μm polyimide film sample showed no dependence on wave-vector direction.

IV. QUALITATIVE ANALYSIS OF ISTS DATA

In this section we present a brief discussion of the main features of ISTS data from thin films. The purpose is to provide focus for the subsequent theoretical treatment and more detailed data analysis.

A. Data features

Figure 2 shows typical diffracted signal obtained using the *Q*-switched probe variant of the ISTS method. These data are the result of averaging 500 laser shots, and took approximately 15 s to obtain. The oscillations in the data

are due to acoustic oscillations initiated by the crossed excitation pulses. The signal intensity depends on the induced time-dependent material displacements (which are described in more detail in the sections that follow), weighted by the probe pulse intensity envelope which is shown in the inset to Fig. 2. In Fig. 2, the first part (~ 85 ns) of the probe pulse arrives at the sample before the excitation pulse, so there is no signal other than that due to parasitically scattered probe light. The excitation pulses heat the sample and initiate acoustic oscillations which are observed in the data. There is also a nonoscillatory component of the signal due to steady-state thermal expansion in the heated regions of the sample. This component finally decays as thermal diffusion washes away the spatially periodic variation in sample temperature. Thermal decay is not observed in these experiments because at these wave vectors, the time scale for thermal diffusion is much longer than the length of the *Q*-switched probe pulse. Instead, the signal in Fig. 2 disappears as the probe pulse ends. In separate ISTS experiments with microsecond temporal ranges, thermal diffusion rates in bulk samples have been determined.³ In addition, recent experiments have measured thermal diffusion in thin superconducting films using larger excitation wave vectors.⁹

To insure that the signal was due to the presence of the polyimide film, control experiments were performed on uncoated silicon wafers. Although ISTS signals from surface acoustic modes of uncoated metal samples have been observed,¹⁰ we could detect no signal from the silicon surface.

From the data in Fig. 2, one can easily extract the frequency of the surface acoustic wave. A Fourier transform of the data is shown in the main part of Fig. 3. As might be expected from the nature of the time-domain signal, the acoustic response is dominated by one mode with a frequency of 113 ± 2 MHz. The dc component of the transform is not shown but is 30 times larger than the acoustic peak. Shown in the inset of Fig. 3 is the Fourier transform of a diffracted signal taken under identical conditions as the data in Fig. 2 but with only one laser shot—i.e., no averaging. While this spectrum is noisier than the spectrum of the averaged data, the position of the main peak is identical. The extra noise in the inset of Fig. 3 is most likely due to self-mode locking within the one *Q*-switched probe pulse. True one-laser shot experiments are clearly possible, but require a smooth probe pulse temporal profile for best results.

Figure 4 shows ISTS data and its Fourier transform for the same sample at a larger scattering wave vector. Here, it can clearly be seen that there are at least two surface acoustic modes that contribute to the signal. As will be shown later, there are many surface acoustic modes—often called pseudo-Rayleigh modes^{11,12}—which can propagate on a layered medium such as polyimide on silicon. For a given system, the number of possible modes depends only on the value of the acoustic wave vector times the thickness of the film layer.¹¹ This fact allows for a comprehensive analysis utilizing data from samples with different film thickness.

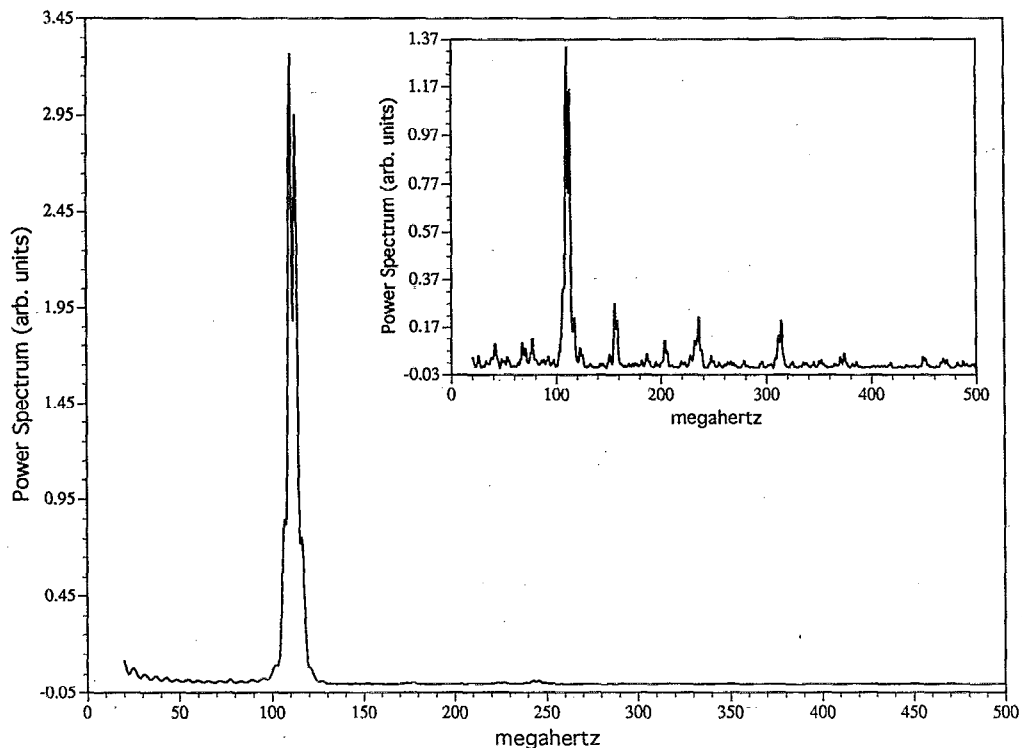


FIG. 3. Fourier transform of the ISTS data of Fig. 2. One peak at 113 ± 2 MHz is clearly resolved. Inset shows the Fourier transform of data taken on the same sample and with the same wave vector as in Fig. 2 but with only one pump-probe laser shot sequence. The strongest peak at 113 ± 2 MHz is identical to that found for the averaged data.

B. Probe diffraction

There are two possible mechanisms for the diffraction of light from pseudo-Rayleigh modes. These are diffraction due to modulation of the dielectric constant through elasto-optic coupling, and diffraction due to surface and interface "ripple" displacements induced by the acoustic motion.¹³ For bulk samples, only the former mechanism is active. For thin supported films, Brillouin scattering studies have shown that both mechanisms can contribute to signal.⁷

Experimentally, it is possible to distinguish between these two scattering mechanisms through analysis of the polarization properties of the diffracted light and the acoustic wave-vector dependence of the diffracted signal intensity. Pseudo-Rayleigh waves have both transverse and longitudinal character,¹¹ and therefore give rise to modulation of both diagonal and off-diagonal elements of the dielectric tensor of a thin film through elasto-optic coupling. If elasto-optic coupling is a significant source of diffraction, then a component of the diffracted probe beam should be polarized at an angle of 90° relative to the incident probe beam (depolarized or *VH* scattering). The magnitude of this component relative to the nondepolarized diffracted component depends on the square of the ratio of off-diagonal to the diagonal elasto-optic coupling coefficients.¹⁴ By contrast, for a coplanar scattering geometry surface ripple does not rotate the polarization of the diffracted light.¹³

In addition, if elasto-optic coupling were the dominant diffraction mechanism, the signal intensity would be independent of scattering wave vector q since the acoustic strain induced through bulk ISTS excitation is q independent.^{2,3} By contrast, surface ripple arises from components of the acoustic displacement rather than strain and should thus vary as q^{-1} . Signal from surface ripple depends on the square of the displacement, and as detailed in Sec. V the signal intensity due to surface ripple decreases as q^{-2} .

We could detect no depolarized component of the diffracted signal. We also observed that the diffracted signal intensity decreases sharply as the q is increased. This indicates that our diffracted signals are due predominantly to surface and interface ripple induced by the pseudo-Rayleigh waves.

C. Surface ripple amplitude

An order-of-magnitude estimate can be made for the surface ripple generated in an ISTS experiment by calculating the magnitude of the temperature grating set up by the excitation laser pulses and then relating this to a displacement amplitude using the linear thermal-expansion coefficient. The temperature change ΔT for light impinging on the surface (in the $y = -h$ plane) in the y direction and setting up a grating of wave vector q in the z direction can be written

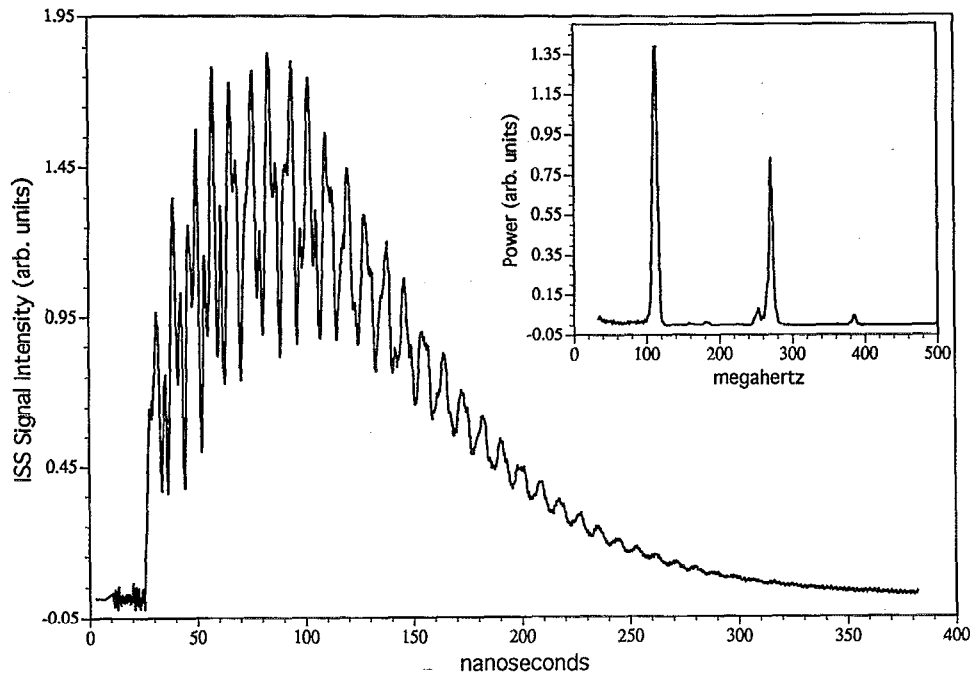


FIG. 4. Diffracted ISTS signal and Fourier transform (inset) for a $5.81 \mu\text{m}$ Pyralin 2555 film on a silicon substrate with an acoustic wave vector of $0.60 \mu\text{m}^{-1}$. The signal is the result of averaging over 500 pump-probe sequences, and it clearly illustrates the existence of multiple modes.

$$\Delta T(y,z) = Ae^{-\zeta y}(1 + e^{iqz}), \quad (2)$$

$$A = (1/\rho C)P_a(1-R)I_E \zeta e^{-\zeta h}, \quad (3)$$

where 2.303ζ is the material absorption coefficient, I_E is the total energy per unit area of the excitation laser pulses, ρ is the mass density, C is the heat capacity per unit mass, R is the reflectivity for the material/air interface, and P_a is the fraction of absorbed light that is converted to heat. An upper limit for the average value of the temperature increase over the thickness of the film can be estimated with Eq. (2) by setting $P_a=1$ and $R=0$. For these experiments, $I_E=16 \text{ mJ/cm}^2$ and $\zeta=1.3 \mu\text{m}^{-1}$. Using values of $\rho=1 \text{ g/cm}^3$ and $C=2.3 \text{ J/(g K)}$ which are typical for polymers¹⁵ leads to an average temperature increase of approximately 8 K for a $4\text{-}\mu\text{m}$ -thick film.

This temperature change can be related to the change in the y -direction length of a volume element $\delta L_y(y,z)$ using the linear thermal-expansion coefficient α_T as in

$$\delta L_y(y,z) = \alpha_T \Delta T(y,z) dy. \quad (4)$$

For the general case, the total surface ripple $R_{\text{rip}}(z)$ can be found by integrating this expression over the sample thickness. In these experiments, the silicon substrate does not absorb the 355 nm excitation light so the integration only extends over the thickness h of the thin film. Performing this integration leads to

$$R_{\text{rip}}(z) = (1/\rho C)P_a(1-R)I_E(1 - e^{-\zeta h})\alpha_T(1 + e^{iqz}). \quad (5)$$

Using a typical polymeric value of $\alpha_T=80 \times 10^{-6} \text{ m/(m K)}$ (Ref. 16) for the linear thermal-expansion coefficient yields an upper-limit estimate of $0.005 \mu\text{m}$ for the surface corrugation amplitude excited by ISTS. This esti-

mation assumes that neighboring volume elements slide by one another, and does not consider the effects of stress that will tend to reduce the corrugation. For this reason, expression (5) does not show the expected $1/q$ dependence.

V. THEORY

In order to extract the elastic constants of the thin film from the pseudo-Rayleigh mode frequencies measured at different scattering wave-vector magnitudes q , it is necessary to understand the dispersion of $\omega(q)$ for the various modes. In fact, the phase velocity depends only on the product qh , where h is the film thickness, so that the results of measurements on films of different thickness can be compared. As mentioned earlier, it is also necessary to

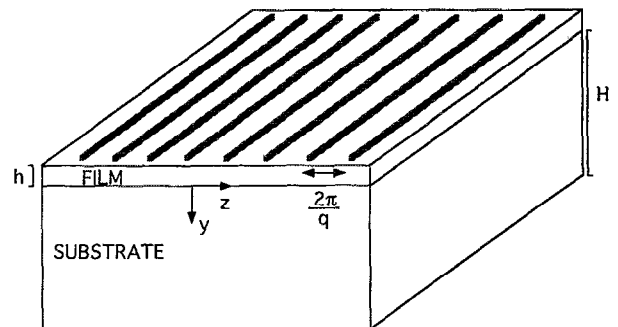


FIG. 5. System geometry used in all theoretical calculations. The film fills the space between $y=0$ and $y=-h$ and the substrate fills the area from $y=0$ to $y=+H$. The acoustic wave-vector setup by the pump beams is in the z direction.

know the ISTS excitation efficiencies and the probe diffraction efficiencies for each of the modes. The theory for acoustic wave propagation in layered media is well known.¹¹ Here we will derive the ISTS signal expected from a supported film treating first the excitation then the probing process. For simplicity we will use an isotropic theory since no effects of the elastic anisotropy of silicon or the film were observed.

A. ISTS excitation of the system

We start with the equations of thermoelasticity for an isotropic, elastic, and homogeneous medium,¹⁷

$$c_{44}\nabla^2\mathbf{u} + (c_{11} - c_{44})\nabla(\nabla\cdot\mathbf{u}) = \gamma\nabla T + \rho \frac{\partial^2\mathbf{u}}{\partial t^2}, \quad (6)$$

$$\kappa\nabla^2 T - C_s\rho \frac{\partial T}{\partial t} - \eta\kappa\nabla\cdot\frac{\partial\mathbf{u}}{\partial t} = -Q. \quad (7)$$

In these expressions, \mathbf{u} is a vector describing the material displacements, T is the fluctuation in temperature relative to the equilibrium temperature, ρ is the equilibrium density, and c_{44} and c_{11} are the elastic constants which are related to the bulk longitudinal and transverse acoustic velocities according to $v_L = (c_{11}/\rho)^{1/2}$ and $v_T = (c_{44}/\rho)^{1/2}$. γ is a constant related to the elastic constants and the coefficient of linear volume expansion α_T by $\gamma = (3c_{11} - 4c_{44})\alpha_T$. κ is the thermal conductivity, $\eta = \gamma T_0/\kappa$, and C_s is the constant strain specific heat per unit mass. Finally, Q represents the absorbed heat per unit time per unit volume derived from the excitation laser pulses.

If one expresses \mathbf{u} in terms of longitudinal (ϕ) and transverse Ψ potentials,

$$\mathbf{u} = \nabla\phi + \nabla\times\Psi, \quad \nabla\cdot\Psi = 0 \quad (8)$$

then Eqs. (6) and (7) can be written as follows:

$$\kappa\nabla^2 T - C_s\rho \frac{\partial T}{\partial t} = -Q, \quad (9)$$

$$\nabla^2\phi - \frac{\rho}{c_{11}} \frac{\partial^2\phi}{\partial t^2} = \frac{\gamma}{c_{11}} T, \quad (10)$$

$$\nabla^2\Psi - \frac{\rho}{c_{44}} \frac{\partial^2\Psi}{\partial t^2} = 0. \quad (11)$$

Here we have also assumed that longitudinal compressions do not cause substantial changes in temperature [$\eta \sim 0$ in Eq. (7)].

Note that for a bulk system, the last two equations describe uncoupled longitudinal and transverse acoustic modes, respectively. It is clear that since the laser heating enters through Eq. (9), which is only directly coupled to Eq. (10), ISTS only excites longitudinal acoustic modes in bulk isotropic systems. However, this simple picture breaks down for a thin film, since boundary conditions must be satisfied. In particular, for a thin film in intimate contact with a substrate, the material displacements and the normal components of the stress must be continuous across the interface and the normal components of the stress at any free surface must vanish. These boundary conditions lead to coupling between the longitudinal and transverse potentials so that every surface acoustic mode has both longitudinal and transverse character.

The film/substrate system geometry is depicted in Fig. 5. The substrate fills the region from $y=0$ to $y=+H$ and the film fills the region from $y=0$ to $y=-h$. It is assumed that the ISTS excitation beams form an infinite uniform grating pattern with wave vector \mathbf{q} in the z direction which is independent of x and damped along y due to optical absorption. In this analysis, H is considered infinite so that the substrate fills the whole $y > 0$ half-space. The Appendix demonstrates the corrections that occur when the finite size of the substrate is explicitly accounted for.

The first step in solving Eqs. (9)–(11) is to determine the temperature distribution set up by the excitation pulses. The dynamics of thermal diffusion take place on a much longer time scale than the acoustic dynamics. Thus, for analyzing the excitation of the film-substrate system, κ can be set to zero in Eq. (9). In ISTS, the excitation laser pulse duration is short compared to the acoustic oscillation period. Here we assume that conversion of optical energy to heat through molecular electronic and vibrational relaxation also occurs on a fast time scale relative to the acoustic oscillation period so that the time dependence of Q in Eq. (9) can be approximated by a δ function at zero time. More gradual thermalization will reduce all the acoustic amplitudes but should not affect the relative amplitudes of the different modes substantially. Equation (9) is solved for the temperature distribution set up by the laser excitation beams to yield

$$T(y,z,t) = Ae^{-\zeta(y+h)}(1 + e^{iqz})\theta(t), \quad (12)$$

where $\theta(t)$ is the Heaviside step function that turns on at $t=0$, and A and ζ were introduced in Eqs. (2) and (3). Since the film absorbs strongly and the silicon substrate reflects the 355 nm excitation light used in these experiments, $T(y,z,t)$ is only nonzero in the film (for $-h < y < 0$).

With this functional form for the temperature distribution, Eqs. (10) and (11) can be solved using transform

techniques. Since the temperature distribution is independent of x , all derivatives with respect to x are neglected. From the geometry of the system and the nature of the temperature distribution given in Eq. (12), a Laplace

transform for the time variable and an exponential Fourier transform for the z coordinate are the natural choices. The transformed solutions for the potentials ϕ and Ψ are then found to be

$$\phi(k,y,s) = \begin{cases} A_\phi(k,s)\exp[y\sqrt{k^2+(s^2/v_{Lf}^2)}] + B_\phi(k,s)\exp[-y\sqrt{k^2+(s^2/v_{Lf}^2)}] \\ + \frac{A\gamma}{\rho s} e^{-\xi y} \left(\frac{\delta(k)}{-s^2 + \xi^2 v_{Lf}^2} + \frac{\delta(k-q)}{-k^2 v_{Lf}^2 + \xi^2 v_{Lf}^2 - s^2} \right), & -h < y < 0, \\ C_\phi(k,s)\exp[y\sqrt{k^2+(s^2/v_{Ls}^2)}] + D_\phi(k,s)\exp[-y\sqrt{k^2+(s^2/v_{Ls}^2)}], & H > y > 0, \end{cases} \quad (13)$$

$$\Psi(k,y,s) = \begin{cases} A_\Psi(k,s)\hat{x}\exp[y\sqrt{k^2+(s^2/v_{Tf}^2)}] + B_\Psi(k,s)\hat{x}\exp[-y\sqrt{k^2+(s^2/v_{Tf}^2)}], & -h < y < 0, \\ C_\Psi(k,s)\hat{x}\exp[y\sqrt{k^2+(s^2/v_{Ts}^2)}] + D_\Psi(k,s)\hat{x}\exp[-y\sqrt{k^2+(s^2/v_{Ts}^2)}], & H > y > 0, \end{cases} \quad (14)$$

where k is the Fourier transform variable conjugate to z and s is the Laplace variable conjugate to time. In these expressions, v_{Lf} , v_{Tf} , v_{Ls} and v_{Ts} are the bulk longitudinal and transverse velocities in the film and substrate, respectively. In taking the Laplace transform, the initial conditions that there is no displacement or motion at $t=0$ when the laser pulses first arrive at the sample have been used. Note that choosing the only nonzero component of Ψ to lie along the x axis allows for trivial satisfaction of the gauge ($\nabla \cdot \Psi = 0$) used here. Finally, all but the third term in the expression for the longitudinal potential in the film are homogeneous solutions to the equations of motion. This third term is the particular solution of Eq. (10) and can be thought of as driving the motion of the film and giving rise to a response consisting of a longitudinal disturbance propagating along z , a periodic stress pulse propagating along y , and a dc response.

The variables $A_\phi(k,s)$, $B_\phi(k,s)$, $D_\phi(k,s)$, etc. are potential constants that are determined by imposing the necessary boundary conditions and physical realizability requirements. For the system of Fig. 5 with H infinite and for phase velocities less than v_{Ts} , the terms involving $C_\phi(k,s)$ and $C_\Psi(k,s)$ represent physically unreasonable solutions. For this reason, they are set to zero. The other six constants are determined with the boundary conditions. As stated earlier, these are that \mathbf{u} and the normal components of the stress are continuous at $y=0$ and that the normal components of the stress vanish for $y=-h$. The stress tensor is calculated using the Duhamel-Neumann relation shown in Eq. (15) in order to properly take into account the contribution from the temperature grating:

$$\sigma_{ij} = c_{44} \left(\frac{\partial u_i}{\partial x_j} + \frac{\partial u_j}{\partial x_i} \right) + [(c_{11} - 2c_{44}) \nabla \cdot \mathbf{u} - \gamma T] \delta_{ij}. \quad (15)$$

Using Eqs. (8), (15), and (12)–(14), the boundary conditions can be imposed. The six relations thus derived are most conveniently expressed in matrix form,

$$\mathbf{CD} = \mathbf{F}, \quad (16)$$

where

$$\mathbf{C} = \begin{pmatrix} (1+p^2)e^{-nkh} & (1+p^2)e^{nkh} & 2ipe^{-pkh} & -2ipe^{pkh} & 0 & 0 \\ 2ine^{-nkh} & -2ine^{nkh} & -(1+p^2)e^{-pkh} & -(1+p^2)e^{pkh} & 0 & 0 \\ 1+p^2 & 1+p^2 & 2ip & -2ip & -(1+r^2)g & 2irg \\ 2in & -2in & -(1+p^2) & -(1+p^2) & 2img & (1+r^2)g \\ -1 & -1 & -ip & ip & 1 & -ir \\ in & -in & -1 & -1 & im & 1 \end{pmatrix}, \quad (17)$$

$$\mathbf{D} = \begin{pmatrix} A_\phi \\ B_\phi \\ A_\psi \\ B_\psi \\ D_\phi \\ D_\psi \end{pmatrix},$$

(18)

$$\mathbf{F} = \frac{iA\gamma}{v_{Tf}^2 \rho k v} \begin{pmatrix} -\frac{[\delta(k) + \delta(k-q)]}{k^2} + \frac{v_{Lf}^2}{k^2} \left(\frac{-(v_{Lf}^2 - 2v_{Tf}^2)}{v_{Lf}^2} + \frac{\xi^2}{k^2} \right) \left(\frac{\delta(k)}{v^2 + (v_{Lf}^2 \xi^2/k^2)} + \frac{\delta(k-q)}{v^2 + v_{Lf}^2 [(\xi^2 - k^2)/k^2]} \right) \\ \frac{2\xi v_{Tf}^2}{ik^3} \left(\frac{\delta(k)}{v^2 + (v_{Lf}^2 \xi^2/k^2)} + \frac{\delta(k-q)}{v^2 + v_{Lf}^2 [(\xi^2 - k^2)/k^2]} \right) \\ -\frac{e^{-\xi d} [\delta(k) + \delta(k-q)]}{k^2} + \frac{e^{-\xi d} v_{Lf}^2}{k^2} \left(\frac{-(v_{Lf}^2 - 2v_{Tf}^2)}{v_{Lf}^2} + \frac{\xi^2}{k^2} \right) \left(\frac{\delta(k)}{v^2 + (v_{Lf}^2 \xi^2/k^2)} + \frac{\delta(k-q)}{v^2 + v_{Lf}^2 [(\xi^2 - k^2)/k^2]} \right) \\ \frac{2e^{-\xi d} \xi v_{Tf}^2}{ik^3} \left(\frac{\delta(k)}{v^2 + (v_{Lf}^2 \xi^2/k^2)} + \frac{\delta(k-q)}{v^2 + v_{Lf}^2 [(\xi^2 - k^2)/k^2]} \right) \\ -\frac{e^{-\xi d} v_{Tf}^2}{k^2} \left(\frac{\delta(k)}{v^2 + (v_{Lf}^2 \xi^2/k^2)} + \frac{\delta(k-q)}{v^2 + v_{Lf}^2 [(\xi^2 - k^2)/k^2]} \right) \\ \frac{e^{-\xi d} \xi v_{Tf}^2}{k^3} \left(\frac{\delta(k)}{v^2 + v_{Lf}^2 \xi^2/k^2} + \frac{\delta(k-q)}{v^2 + v_{Lf}^2 [(\xi^2 - k^2)/k^2]} \right) \end{pmatrix},$$

(19)

$$n = \sqrt{1 - (v^2/v_{Lf}^2)}, \quad (20)$$

$$p = \sqrt{1 - (v^2/v_{Tf}^2)}, \quad (21)$$

$$m = \sqrt{1 - (v^2/v_{Ls}^2)}, \quad (22)$$

$$r = \sqrt{1 - (v^2/v_{Ts}^2)}, \quad (23)$$

$$g = \rho_s v_{Ts}^2 / \rho_f v_{Tf}^2 \quad (24)$$

and ρ_f and ρ_s are the densities in the film and substrate, respectively. The first two rows of the matrix equation ensure that the yy and the yz components of the stress, respectively, are zero at the surface of the film. The next two rows require continuity of the yy and yz components of the stress, respectively, at the interface. Finally, the last two rows require that the z and y components of the material velocities, respectively, are continuous at the interface. For notational convenience, the k and s dependence of the potential constants has been dropped. Also, the Laplace variable s has been written as $s^2 = -\omega^2 = -v^2 k^2$, where ω is the real frequency and v is the phase velocity of the acoustic mode solutions. This transformation limits the possible solutions to strictly pseudo-Rayleigh modes with velocities below the transverse velocity of the substrate. A continuum of "leaky mode" solutions with complex frequency are also possible for velocities greater than v_{Ts} .¹⁸ These solutions are damped as energy is "lost" to the semi-infinite substrate. Normal mode solutions of Eq. (16) occur when

$$\det(\mathbf{C}) = 0. \quad (25)$$

Aside from kh and v , and the matrix \mathbf{C} only contains constants related to the thin film and the substrate. All of the laser and optical properties appear in the column matrix \mathbf{F} . Thus Eq. (25) can be solved to yield the dispersion relations (qh vs v , where q is the acoustic wave vector) for the various pseudo-Rayleigh modes irrespective of the ISTS excitation source.

An example of typical dispersion curves for the substrate loading case (i.e., $v_{Ts} > v_{Tf}$) is shown for the lowest 16 modes in Fig. 6. As qh approaches zero only one mode, whose velocity approaches that of the substrate pure Rayleigh mode v_{Rs} , exists. At large qh , this lowest mode becomes the pure Rayleigh surface mode of the film with velocity v_{Rf} . Each of the higher-velocity modes, often called Sezawa modes, has a limiting qh value below which it does not propagate. At this qh value, the velocity of each mode is equal to the substrate transverse velocity v_{Ts} . As shown in Fig. 6, as qh is increased, these modes all asymptotically approach the film transverse velocity.

In order to solve for the displacements of a particular mode j excited through ISTS, one must solve the full Eq. (16) for the potential constants at the qh value and velocity of interest. It can be shown using Eqs. (8) and (13)–(14) that the normal mode displacements \mathbf{u}^j with wave vector q obey the following equation:

$$\mathbf{u}^j(q, y, z, t) = [u_y^j(q, y) \hat{\mathbf{y}} + u_z^j(q, y) \hat{\mathbf{z}}] e^{iqz} e^{i\omega_j t}, \quad (26)$$

where

$$u_y^j(q,y) = \begin{cases} qn_j(\tilde{A}_\phi^j e^{yqn_j} - \tilde{B}_\phi^j e^{-yqn_j}) + iq(\tilde{A}_\psi^j e^{yqp_j} + \tilde{B}_\psi^j e^{-yqp_j}), & -h < y < 0, \\ -qm_j \tilde{D}_\phi^j e^{-yqm_j} + iq \tilde{D}_\psi^j e^{-yqr_j}, & y > 0, \end{cases} \quad (27)$$

$$u_z^j(q,y) = \begin{cases} iq(\tilde{A}_\phi^j e^{yqn_j} + \tilde{B}_\phi^j e^{-yqn_j}) + qp_j(-\tilde{A}_\psi^j e^{yqp_j} + \tilde{B}_\psi^j e^{-yqp_j}), & -h < y < 0, \\ iq \tilde{D}_\phi^j e^{-yqm_j} + qr_j \tilde{D}_\psi^j e^{-yqr_j}, & y > 0. \end{cases} \quad (28)$$

In these expressions, the tildes denote the residue of the quantity evaluated at the appropriate pole. Note that the material displacements oscillate with frequency $\omega_j = v_j q$. Examples of the pseudo-Rayleigh displacements for various modes at one qh value are shown in Fig. 7. The total displacement at a particular wave vector and sample thickness will be the sum of the u^j values for each pseudo-Rayleigh mode plus a nonoscillatory term due to steady-state thermal expansion.

B. Probe diffraction

A complete treatment of the diffraction of light from pseudo-Rayleigh waves in thin supported films which includes both elasto-optic and surface corrugation effects has been presented by Bortolani *et al.*¹³ in the context of Brillouin scattering. In this subsection, we present a simplified analysis appropriate for the ISTS experiments described here in which ripple effects were found to dominate. We start with results derived by Lean¹⁹ for the reflected and transmitted first-order diffracted components of light from a corrugated half-space. These expressions are modified to deal with the case of arbitrary indices of refraction on either side of the corrugated interface, and to the case of

standing-wave corrugation. In addition, index modulation contributions to the phase are neglected. The results are

$$E_r = \mp \hat{a} \sqrt{I_0} e^{i\omega t} e^{-in_1 k_i R_0} J_1(\alpha_1) \times \left(\frac{[1+r(\theta_1)] \cos \theta_d - [1-r(\theta_1)] \cos \theta_i}{2 \cos \theta_i} \pm \frac{q[1+r(\theta_1)] (\sin \theta_d + \sin \theta_i)}{2n_1 k_i \cos \theta_i (\cos \theta_d + \cos \theta_i)} \right), \quad (29a)$$

$$\alpha_1 = \delta(t) n_1 k_i (\cos \theta_d + \cos \theta_i), \quad (29b)$$

$$\sin \theta_{d\pm 1} = \sin \theta_i \pm (q/n_1 k_i), \quad (29c)$$

$$E_t = \mp \hat{a} \sqrt{I_0} e^{i\omega t} e^{-in_2 k_i R_0/n_1} J_1(\alpha'_1) \times \left(\frac{[1+r(\theta_i)] (n_2/n_1) \cos \theta_i + [1-r(\theta_i)] \cos \theta_i}{2 \cos \theta_i} \mp \frac{q[1+r(\theta_i)] [(n_2/n_1) \sin \theta_i + \sin \theta_i]}{2n_1 k_i \cos \theta_i [(n_2/n_1) \cos \theta_i - \cos \theta_i]} \right), \quad (30a)$$

$$\alpha'_1 = \delta(t) n_1 k_i [(n_2/n_1) \cos \theta_i - \cos \theta_i], \quad (30b)$$

$$\sin \theta_{i\pm 1} = (n_1/n_2) \sin \theta_i \pm (q/n_2 k_i). \quad (30c)$$

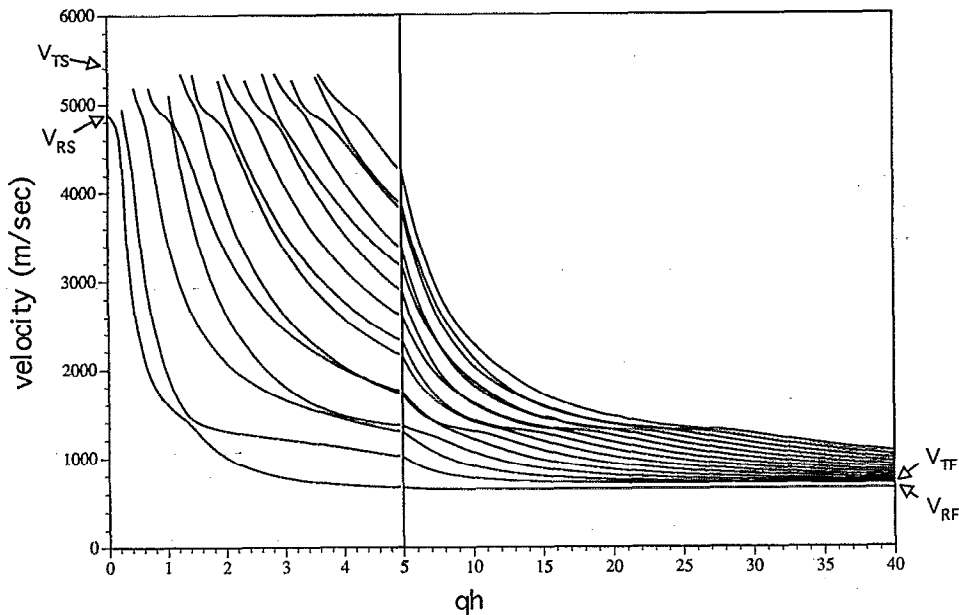


FIG. 6. Pseudo-Rayleigh mode dispersion generated using substrate elastic parameters $v_{Ls}=8945$ m/s, $v_{Ts}=5341$ m/s, $\rho_s=2.33$ g/cm³, and film elastic parameters $v_{Lf}=1300$ m/s, $v_{Tf}=700$ m/s, $\rho_f=1.45$ g/cm³. The acoustic wave vector is given by q , the film thickness is h , and v_{Rs} and v_{Rf} are the substrate and film Rayleigh surface velocities, respectively.

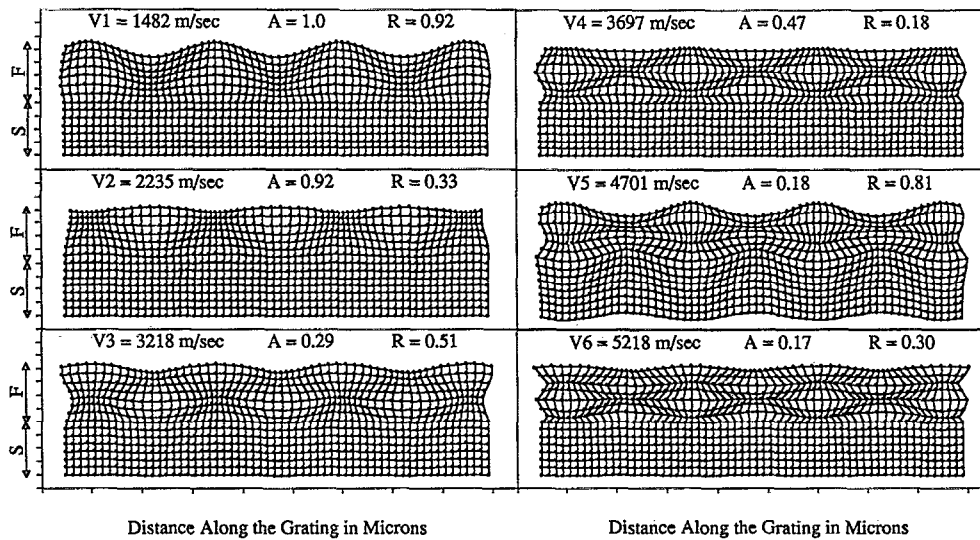


FIG. 7. Material displacements for the first six pseudo-Rayleigh modes that propagate on a $1 \mu\text{m}$ film (F) coating an infinite substrate (S) at a qh value of 2.5. The displacements were calculated for the film layer and to a depth of $1 \mu\text{m}$ into the substrate using the best-fit elastic constants listed in the caption of Fig. 12. The scale factors (A) for each mode are determined such that the largest component of displacement in the mode that is driven most efficiently is equal to one. The ripple amplitude (R) for each mode is given relative to the maximum displacement amplitude for that mode.

In these equations, I_0 is the intensity of the probe measured in medium 1, and k_i is the wave vector of the probe measured in vacuum; θ_i is the angle of the probe relative to the corrugated interface, a is the unit vector representing the polarization of the probe, r is the reflection coefficient for transmission from medium 1 to medium 2, and R_0 is the distance from the point at which the diffraction is generated to the detector. Also, q is the wave vector of the corrugation and $\delta(t)$ is the time-dependent amplitude of the corrugation. Finally, the upper signs refer to the $+1$ diffracted order, while the lower signs refer to the -1 diffracted order.

For a thin supported film, there are four sources of first-order ripple diffraction which must be considered. These are shown schematically in Fig. 8. Parts (a) and (b) of this figure represent the probe and diffracted beam paths for the two final signal directions seen experimentally. The first three paths show the components involving diffraction from the film surface ripple. The fourth path describes the component arising from diffraction from the interface ripple. In general, all four components contribute to the diffracted signal in the two signal directions.

The electric fields at the detector associated with these four diffraction contributions can be obtained using Eqs. (29) and (30), Snell's law, and taking into account reflective losses at the film-air interface. In the following, it is assumed that all light striking the film-substrate interface is reflected. In addition, due to the spatial size of the probe pulse, the thickness of the film, the index of refraction of the film, the wave vector of the corrugation, and the angle of incidence, it is a good approximation to assume that all of the diffracted beams given in Figs. 8(a) or 8(b) emerge from the same point on the film and travel parallel to one another. The results, written in terms of sums over pseudo-

Rayleigh mode amplitudes, are shown in the following equations:

$$E_1 = \mp \hat{a} \sqrt{I_0} K_1 e^{i\omega t - ik_i R_0} \sum_{j=0}^N u_j y(q, y = -h) \sin(v_j q t), \quad (31a)$$

$$K_1 = k_i (\cos \theta_d + \cos \theta_i) \times \left(\frac{[1 + r(\theta_i)] \cos \theta_d - [1 - r(\theta_i)] \cos \theta_i}{4 \cos \theta_i} \pm \frac{q [1 + r(\theta_i)] (\sin \theta_d + \sin \theta_i)}{4 k_i \cos \theta_i (\cos \theta_d + \cos \theta_i)} \right), \quad (31b)$$

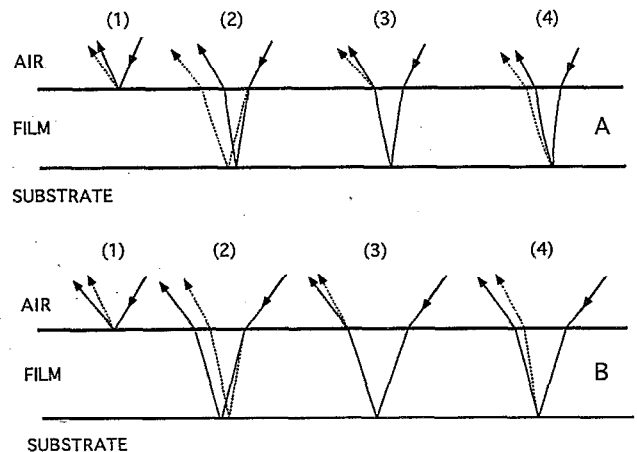


FIG. 8. Schematic illustration of the beam paths for the four components of first-order ripple diffraction that contribute to ISTS signal. Parts (A) and (B) describe the different paths for the two final signal directions observed experimentally.

$$\sin \theta_{d\pm 1} = \sin \theta_i \pm (q/k_i), \quad (31c)$$

$$E_2 = \mp \hat{a}t'(\theta_i) \sqrt{I_0} K_2 e^{i\omega t} e^{-ik_x R_0} e^{-ink_y h_2} \times \sum_{j=0}^N u_y^j(q, y = -h) \sin(v_j q t), \quad (32a)$$

$$K_2 = k_i (n \cos \theta_i - \cos \theta_i) \times \left(\frac{[1+r(\theta_i)] n \cos \theta_i + [1-r(\theta_i)] \cos \theta_i}{4 \cos \theta_i} \mp \frac{q[1+r(\theta_i)] (n \sin \theta_i + \sin \theta_i)}{4k_i \cos \theta_i (n \cos \theta_i - \cos \theta_i)} \right), \quad (32b)$$

$$\sin \theta_{i\pm 1} = (1/n) \sin \theta_i \pm (q/nk_i), \quad (32c)$$

$$h_2 = 2h / \cos \theta_{i\pm 1}, \quad (32d)$$

$$E_3 = \mp \hat{a}t(\theta_i) \sqrt{I_0} K_3 e^{i\omega t} e^{-ik_x R_0} e^{-ink_y h_3} \times \sum_{j=0}^N u_y^j(q, y = -h) \sin(v_j q t), \quad (33a)$$

$$K_3 = k_i (\cos \theta_i - n \cos \theta_{rfr}) \times \left(\frac{[1+r'(\theta_{rfr})] \cos \theta_i + n[1-r'(\theta_{rfr})] \cos \theta_{rfr}}{4 \cos \theta_{rfr}} \mp \frac{q[1+r'(\theta_{rfr})] (\sin \theta_i + n \sin \theta_{rfr})}{4k_i \cos \theta_{rfr} (\cos \theta_i - n \cos \theta_{rfr})} \right), \quad (33b)$$

$$\sin \theta'_{i\pm 1} = n \sin \theta_{rfr} \pm (q/k_i), \quad (33c)$$

$$h_3 = 2h / \cos \theta_{rfr}, \quad (33d)$$

$$\theta_{rfr} = \sin^{-1} [(1/n) \sin \theta_i], \quad (33e)$$

$$E_4 = \mp \hat{a}t(\theta_i) t'(\theta'_d) \sqrt{I_0} K_4 e^{i\omega t} e^{-ik_x R_0} e^{-ink_y h_4} \times \sum_{j=0}^N u_y^j(q, y = 0) \sin(v_j q t), \quad (34a)$$

$$K_4 = nk_i (\cos \theta'_d + \cos \theta_{rfr}) \times \left(\frac{n \cos \theta'_d \pm q (\sin \theta'_d + \sin \theta_{rfr})}{2 \cos \theta_{rfr} \pm 2k_i \cos \theta_{rfr} (\cos \theta'_d + \cos \theta_{rfr})} \right), \quad (34b)$$

$$\sin \theta'_{d\pm 1} = \sin \theta_{rfr} \pm (q/nk_i), \quad (34c)$$

$$h_4 = (h / \cos \theta_{rfr}) + (h / \cos \theta'_{d\pm 1}), \quad (34d)$$

where j runs from 0 to N and represents the mode solutions for $j > 0$ and the dc term for $j = 0$ (i.e., $v_0 = 0$), t is the transmission coefficient for passage from the air into the film, and t' is the transmission coefficient for passage from the film into the air. Finally, in these expressions the small-argument expansion of the Bessel function [$J_1(x) \sim x/2$ for $x \ll 1$] has been used since the ripple amplitude (as estimated in Sec. IV) times the grating wave-vector magnitude is small compared to one for all excitation geometries investigated in this experiment.

The signal intensity can be written as the square of the sum of the four electric fields given in Eqs. (31)–(34). The resulting intensity will exhibit varying interference effects depending on the probing angle and wavelength, the index of refraction and thickness of the film, and the grating excitation wave vector. For the purpose of analyzing the relative intensities of the various pseudo-Rayleigh modes in an ISTS experiment, the only important interference occurs between the E fields derived from the surface ripple (E_1 – E_3) and the field derived from the interface ripple (E_4). Such interference can cause a mode with a large surface corrugation amplitude to only appear as a weak Fourier component in the experimentally measured diffraction signal and vice versa. The final ISTS intensity I can be written in a manner which emphasizes this effect as

$$I = I_0 \left(\sum_j \{ [F(n, h, k_i, q, \theta_i) u_y^j(q, y = -h) + G(n, h, k_i, q, \theta_i) u_y^j(q, y = 0)] \sin(v_j q t) \} \right) \text{c.c.}, \quad (35)$$

where c.c. denotes complex conjugate, and where F and G are functions determined by summing terms in Eqs. (31)–(34). This expression was obtained by averaging over an optical cycle with the assumption that acoustic terms are constant over this interval. One can see that, in general, the measured signal consists of a dc term, a series of heterodyned components oscillating at the pseudo-Rayleigh mode frequencies which arise from a beating against the dc term, and terms oscillating at sums and differences of the normal mode frequencies.

C. Qualitative considerations

The relative intensities of the various modes seen with ISTS depend on two factors—the extent to which the different modes are excited by the pump pulses and the efficiency with which the surface and interface mode displacements diffract the probe pulse. Both of these factors can be quantified at a particular qh value by solving the full matrix Eq. (16) for each mode. This was done using the elastic constants found for the polyimide/silicon system as described in Sec. VI. Aside from an overall constant factor, the only additional input parameter needed to perform this computation was the polyimide absorption coefficient ζ . This was measured to be $1.3 \mu\text{m}^{-1}$ using a polyimide film coated onto a fused silica substrate. Figure 7 shows the results of the calculations at $qh = 2.5$. This figure shows material displacements for the first eight modes that exist at this value of qh . The relative excitation efficiencies for the different modes are indicated by the relative amplitudes A ($A = 1$ for the mode with the largest displacements). The surface ripple amplitude relative to the maximum amplitude for each mode is given by R . Modes with large values of the product AR contribute most to ISTS signal. There are several guidelines that can be determined through a study of these and other such figures that allow for an understanding of the level of excitation and the resulting diffraction efficiency of a particular mode. First, modes with fewer spatial modulations along the y direction are

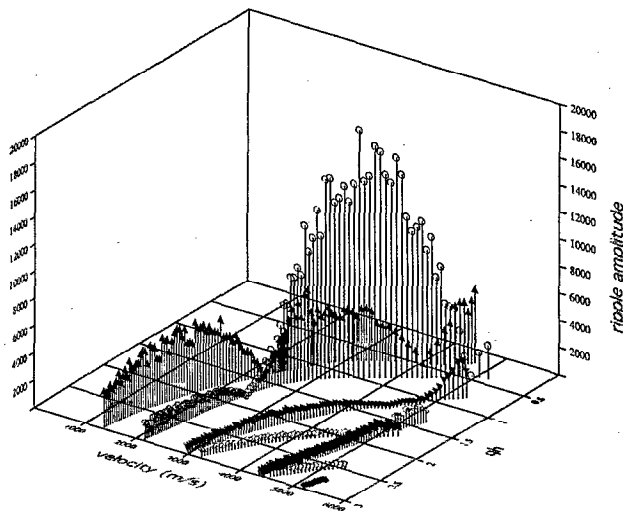


FIG. 9. Plot of the film surface ripple amplitude vs qh and velocity for a given ISTS heat input using the best-fit elastic constants listed in the caption of Fig. 12. Each symbol represents a different mode dispersion curve to facilitate comparison with Fig. 12. The units of the z axis are arbitrary.

excited more strongly than those with many nodes along y . This is reasonable since the heating excitation mechanism will tend to displace material in only one direction for a given value of z . Next, lower-velocity modes in general have larger peak displacements than high velocity modes. This is due to the fact that as the mode velocity is increased and approaches the substrate transverse velocity, the mode displacements become spread out over both the film and far into the substrate. This leads to smaller peak displacement amplitudes compared to those of the low-velocity modes whose displacements are well localized in the film. Finally, it is evident that some modes involve much more surface and interface ripple than others. Since detection results predominantly from diffraction from surface and interface ripple, only modes with significant surface displacements along y are detected. With these guidelines, it is possible to qualitatively explain relative signal amplitudes from the various modes over a wide range of qh . For purposes of data analysis, the calculations provide a clear indication of which modes in a thin film are likely to be observed in ISTS data. In most of our data, only one or two frequency components are observed predominantly. Dispersion curves like those in Fig. 6 can be fit to the frequency values determined from the data, with the elastic moduli as adjustable parameters to be deduced from the best fit. To do this correctly it is essential to know which modes are under observation, i.e., which of the many dispersion curves should be fit to the experimentally determined frequency values.

Figure 7 illustrates bulk and surface ripple amplitudes for a single value of wave vector q , given the film thickness h . Figure 9 is a three-dimensional plot showing the calculated film surface ripple (the product AR) excited through ISTS as a function of qh and velocity for the various modes in a $1 \mu\text{m}$ film. Figure 10 displays the analogous results for

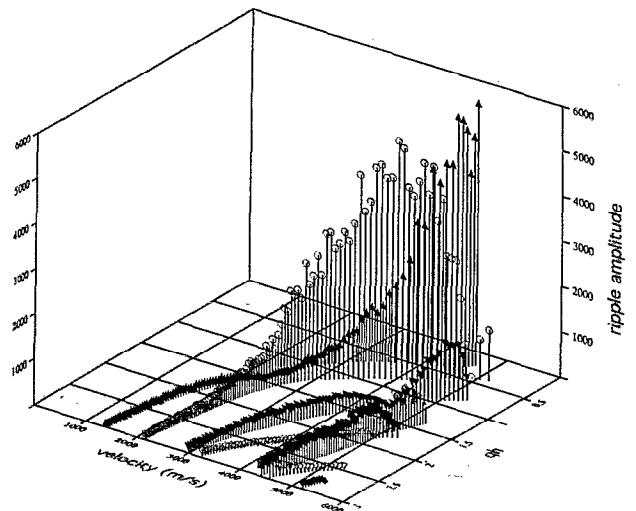


FIG. 10. Plot of the film-substrate interface ripple amplitude vs qh and velocity using the same parameters as Fig. 9. The units of the z axis are the same as those given in Fig. 9.

the interface ripple. The x - y plane of these figures shows the mode velocity dispersion as in Fig. 6, while the z axis shows the relative ripple displacements for a given energy density of the ISTS excitation pulses. Note that since the displacements associated with each pseudo-Rayleigh mode are different, the relative ripple displacements for the film surface and the film-substrate interface are also different. Both, however, exhibit the same general trend of decreasing ripple amplitude with increasing qh . For fixed h as in this simulation, this corresponds to decreasing mode displacement amplitude with increasing wave vector which, as discussed earlier, is expected for ISTS excitation. In addition to this decrease in amplitude, which is approximately like $1/q$ for values of qh above 1, there is a distinct decrease in the magnitude of the surface ripple for small values of q . This decrease is attributed to the fact that as q is decreased to values near zero, even the lowest modes take on large velocities. Thus, as discussed above, these modes are not well localized and so have small peak dis-

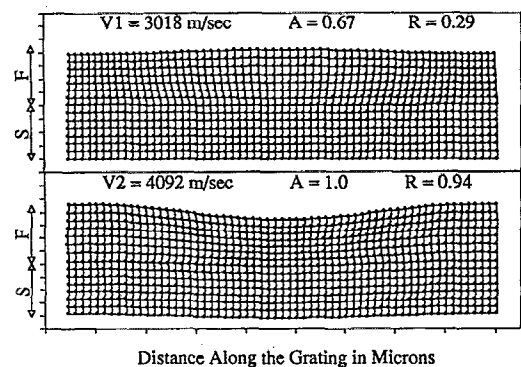


FIG. 11. Lattice distortion figures of the first two modes at $qh=0.8$. Upon comparison of this figure with Fig. 7, the existence of a crossover is apparent.

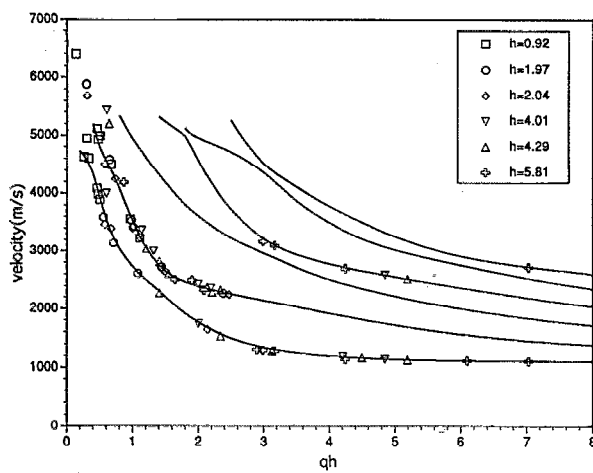


FIG. 12. Experimental data (symbols) and theoretical pseudo-Rayleigh mode dispersion curves (solid lines) for Pyralin 2555 films on silicon substrates with film thicknesses h in micrometers as shown in the legend. The elastic parameters used in generating the dispersion curves were optimized to best fit the data that fall on the two lowest-velocity curves. The substrate parameters used were $v_{Ls}=8945$ m/s, $v_{Ts}=5341$ m/s, $\rho_s=2.33$ g/cm³, and the film parameters determined were $v_{Lf}=2650$ m/s, $v_{Tf}=1160$ m/s, and $\rho_f=1.45$ g/cm³.

placements. For this reason, the ripple due to such modes is small.

In addition to the decrease in surface ripple at both high and very low values of q , it is seen in Fig. 9 that there is a “crossover” near $qh=1.5$ where, upon increase in qh , the surface ripple due to mode two becomes small and that due to mode one becomes large. This occurs because the character of these two modes switch in this region. This “crossover” is evident through a comparison of modes one and two at $qh=2.5$ given in Fig. 7 and at $qh=0.8$ given in Fig. 11, and from the dispersion curves of Fig. 12, in which there is an “avoided crossing” of the first two frequencies.

The relative contribution of each pseudo-Rayleigh mode to the ISTS signal can be calculated using Eq. (16) and the ripple information contained in Figs. 9 and 10. The resulting mode intensity ratios can then be compared to the ratios found in the raw ISTS data for each value of qh and h . When the interface displacements are not negligibly small compared to the surface displacements, interference effects between these two contributions to diffracted signal become important so that with different experimental conditions—such as probe angle of incidence or film thickness—ISTS data can show vastly different mode intensity ratios [see Eq. (35)]. Conversely, when one or the other set of displacements dominates, interference effects can be ignored and the resulting mode intensity ratios become independent of the precise experimental conditions and mimic the behavior of the relevant ripple displacements. From Figs. 9 and 10 and it is clear that the theoretical surface displacements are over an order of magnitude larger than the interface displacements for the two lowest-velocity modes with qh values above ~ 0.5 , while for the other modes and at lower qh , the surface and interface displacements are of the same order. Calculations performed at other film thicknesses between 1 and 5 μm

show this same general behavior. Thus, for the samples examined in this study, one would expect the relative intensities of the two lowest modes to mirror the relative intensities shown in Fig. 9 for $qh > 0.5$, but an analysis of the complete mode intensity spectrum would require the full solution of Eq. (35).

VI. QUANTITATIVE ANALYSIS OF ISTS DATA

As stated earlier, the dc term dominates the ISTS signal for these experiments. In fact the power in the zero-frequency peak of the Fourier transforms ranged from 30 to 200 times greater than the acoustic peaks. Thus, the heterodyne terms in Eq. (35) dominate and the frequencies of the most intense Fourier peaks will correspond to the fundamental pseudo-Rayleigh mode frequencies ω_j .

The values of ω_j found for all the scattering wave vectors and sample thicknesses in this study were converted to phase velocities and plotted versus qh . The results are shown in Fig. 12. In cases where multiple modes were excited, only those with Fourier-transformed intensities greater than half that of the largest peak were plotted. In addition, to eliminate the possibility of spurious peaks due to sample imperfections, data points were taken at several spots on each sample and only frequencies that were consistent from spot to spot on the same sample were kept. The estimated experimental uncertainties for the velocities range from 1% at the highest qh values to 5% at the lowest qh values observed for each sample. The qh values are accurate to ± 0.1 . The main source of error results from uncertainties in the scattering wave vector which are derived from uncertainties in the mechanical measurement of the scattering angle. This error could be substantially reduced in future experiments by deducing the scattering wave vector directly from ISTS data taken with a well-characterized reference sample.

The solution for the pseudo-Rayleigh mode dispersion of this system requires the density and the longitudinal and transverse velocities for both the silicon and the polyimide as inputs. For silicon, $\rho_s=2.33$ g/cm³,²⁰ and the isotropic velocities are $v_{Ls}=8945$ m/s and $v_{Ts}=5341$ m/s.²¹ For polyimide, the values given by Dupont for the density and Young’s modulus Y are 1.45 g/cm³ and 2.4 GPa, respectively.²² To the authors’ knowledge, there is no reported measurement of Poisson’s ratio ν for this film. All three of these values are necessary to obtain the longitudinal and transverse velocities for the film according to

$$v_T^2 = \frac{Y}{2\rho(1+\nu)}, \quad (36)$$

$$v_L^2 = \frac{Y}{\rho(1+\nu)} \left(1 + \frac{\nu}{1-2\nu} \right). \quad (37)$$

Different sets of dispersion curves were generated by solving Eq. (25) using the silicon and polyimide parameters given above and varying Poisson’s ratio for the polyimide from 0 to 0.5. None of these theoretical data sets were able to fit the experimental data adequately.

It was thus decided to fit the experimental data numerically using the Marquardt–Levenberg nonlinear least-

squares algorithm. In performing such a calculation, one must assign each experimental point to a particular dispersion curve. This was fairly straightforward for the data shown in Fig. 12 since the experimental points group together into well-defined curves resembling the pseudo-Rayleigh dispersion curves. The theoretical results shown in Figs. 9 and 10 and discussed above indicate that the two lowest-velocity pseudo-Rayleigh modes should give rise to the strongest signals for most of the wave vectors used. We therefore assumed that the two lowest-velocity sets of data points correspond to the two lowest-velocity pseudo-Rayleigh dispersion curves. The polyimide velocities (v_{Lf} and v_{Tf}) were adjusted to fit the points on these lowest-velocity curves with the density fixed at the previously measured²² value of 1.45 g/cm³. Figure 12 shows the data points and the fit. Using the values obtained, higher-velocity pseudo-Rayleigh dispersion curves were calculated and plotted on Fig. 12. The agreement between these higher-velocity pseudo-Rayleigh dispersion curves and the higher-velocity data points is excellent, with no further adjusting of any parameters.

The polyimide velocity parameters determined from the fit are $v_{Lf}=2650$ m/s and $v_{Tf}=1160$ m/s. While it is never certain that one has reached the global minimum in the value of χ^2 using nonlinear least-squares-fitting routines, these values correspond to the lowest minimum found after starting from many different initial guesses for the parameter values. Varying either of the polyimide velocity parameters by 10% led to substantially worse fits. The fits were relatively insensitive to the value chosen for the polyimide density as changes in this parameter by as much as 50% did not lead to significant changes in the quality of the fits. Varying the substrate parameters by 10% led to worse fits for values of $qh < 1$, but did not affect the quality of the fits at higher qh values. Based on these considerations, we estimate the overall uncertainties in the polyimide velocity parameter values to be $\pm 5\%$.

The outlying high-velocity data points observed are not strictly pseudo-Rayleigh surface modes but rather represent modes that arise from interactions with the free substrate boundary. Their counterparts for the semi-infinite substrate are known as "leaky" modes which are damped due to the fact that they lose energy to the semi-infinite substrate as they propagate.¹⁸ The behavior of these modes can be elucidated by treating the finite size of the substrate explicitly. This is demonstrated in the Appendix.

In these initial experiments, care was not taken to accurately fix or measure the probe angle of incidence θ_i . This precludes a quantitative mode intensity analysis since, according to Eqs. (29)–(34), changes in θ_i significantly change the values of F and G in Eq. (35), which in turn can change the final mode intensities seen in an ISTS experiment. However, as discussed above, the relative intensities of the two lowest modes can be compared to the film surface displacements of Fig. 9 for $qh > 0.5$. Experimentally, Fig. 12 shows that at least one of these two modes is present for all the samples. According to Fig. 9, the second lowest mode should dominate from $qh \sim 0.5$ to $qh \sim 1.5$ while at higher qh values, i.e., above the crossover dis-

cussed earlier, the lowest mode should have a higher intensity. Upon examination of Fig. 12, this qualitative behavior definitely obtains since, for all the samples, the density of observed data points is much higher for the second mode than for the first for qh values less than the crossover, while at higher qh values the only observed data points correspond to the first mode. Further experiments are required in order to more quantitatively test the relative pseudo-Rayleigh mode intensity spectrum predicted for an ISTS experiment according to the method outlined above.

VII. DISCUSSION

The values of $v_{Lf}=2650 \pm 130$ m/s and $v_{Tf}=1160 \pm 60$ m/s deduced in this study for polyimide 2555 combined with the previously measured²² density of 1.45 g/cm³ correspond to a Young's modulus of 5.4 ± 0.5 GPa and a Poisson ratio of 0.38 ± 0.02 . (The uncertainties given for Young's modulus and the Poisson ratio are calculated from the uncertainties for v_{Lf} and v_{Tf} determined from our study and do not account for any uncertainties in the previously measured value for the film density.) To our knowledge, this represents the first measurement of the Poisson ratio in this material. We note that our value for Young's modulus is over 100% higher than the previously measured value²² of 2.4 GPa. This should not be surprising since it is known that the value of Young's modulus can depend very sensitively on the method of film curing. Thus, the difference is probably due to intrinsic differences in sample characteristics.

Recent work has shown that polyimide films can exhibit variation in the degree of chain orientation and in density as a function of depth.^{23–26} Our measurements yield values that are averaged over the film thickness and so do not provide direct information about depth dependencies. It is possible that measurements of thinner films could yield different parameters, indicative of differences in film properties very close to the substrate surface. It may also be possible, for example, by tilting the grating wave vector so that it has a component perpendicular to the film, to determine separate in-plane and out-of-plane elastic moduli. It would then be necessary to generalize the theoretical treatment outlined here to take this into account. At present, the measurements and a simple extension of the theory can be used to determine anisotropic properties within the plane of the film only.

In general, there are several different protocols available for extracting the elastic parameters from ISTS data on thin supported films. One method, which was demonstrated above, involves determining the mode velocities at a range of qh values—by either changing scattering angle or sample thickness or both—and then varying the elastic parameters until a good match between theoretical dispersion curves and data is obtained. With some refinement, especially in the accuracy of the scattering wave-vector measurement, the experimental errors can be reduced and an analysis along these lines should be possible with fewer qh values and higher accuracy. An alternative or comple-

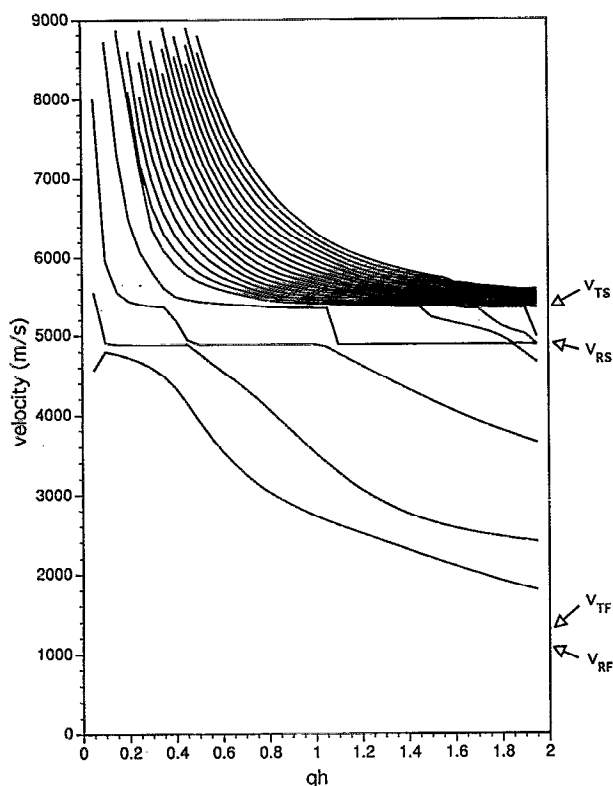


FIG. 13. Dispersion curves for the first 22 normal modes for a $3 \mu\text{m}$ film on a $330 \mu\text{m}$ substrate using the best-fit elastic constants for the polyimide/silicon system listed in Fig. 12. Note the existence of modes with velocities above v_{TS} , which was the cutoff value for the pseudo-Rayleigh modes calculated for an infinite substrate as in Figs. 6 and 12.

mentary method would involve using the relative ISTS signal intensity information obtained for the different modes at each qh value. As discussed earlier, a quantitative analysis of the relative intensities would require accurate specification of the incident probe angle, the indices of refraction of the film and substrate, and the film thickness. The first parameter is easily determined in the ISTS experiment. The indices of refraction and film thickness could be measured by other techniques, or treated as free parameters in a fitting scheme. Ideally it should be possible to extract the elastic parameters using data from only one qh value at which multiple modes are observed, by fitting both the pseudo-Rayleigh mode velocities and relative intensities. With the development of efficient computing algorithms to accomplish this fitting, it should be possible to extract the elastic parameters with the same real-time rates demonstrated here for the data acquisition.

The refinement of "one-shot" data collection, already demonstrated here but not yet optimized, is an important step in either protocol. This should be straightforward as it depends only on an improved probe pulse temporal profile.

VIII. CONCLUSION

In this paper, it has been demonstrated that ISTS experiments with real-time data acquisition rates are possible

and can be applied to studying the pseudo-Rayleigh acoustic modes that propagate in thin-film coatings. Experiments were performed on polyimide films of varying thickness coated onto silicon wafers. For these samples, real-time data acquisition was crucial in avoiding optical damage to the polymer film. It was found that a diffracted ISTS signal arises predominantly from corrugation or ripple displacements at the film surface and the film/substrate interface due to the propagating pseudo-Rayleigh modes. The relative contribution of each acoustic mode to the ISTS signal depends on the efficiency with which each mode is excited by the excitation pulses and on the efficiency with which each mode diffracts the probe beam due to surface and interface ripple. A formalism was developed to quantify both of these factors. Using this formalism a method for extracting the elastic constants of the film by analyzing the dispersion of the pseudo-Rayleigh modes was described and applied to the polyimide/silicon system.

The techniques under development should find wide applications in nondestructive, real-time characterization of thin films. For many applications, such as monitoring thin-film fabrication and cure or determination of the spatial uniformity of coatings, it may not be necessary to determine elastic moduli but merely to monitor changes in acoustic frequency. Finally, real-time characterization of thermal diffusion rates through the use of a probe pulse with a longer temporal duration will present a similar range of applications in polymeric, diamond, and other thin films.

ACKNOWLEDGMENTS

This work was supported in part by NSF Grant No. DMR-9002279, and by contributions from DuPont and Perkin-Elmer. We thank M. Rothschild and M. W. Horn for helpful discussions and C. A. Bukowski for expert technical assistance. J.A.R. acknowledges the support of a NSF doctoral fellowship.

APPENDIX

In this Appendix, the solution for the transient grating excitation of a thin film coating is generalized to include the effects of a substrate with finite thickness. The formal solution for the displacement potentials is still given by Eqs. (13) and (14); however, now the finite substrate has a free boundary at $y=H$ (see Fig. 5) which is ignored for the semi-infinite system. For this reason, the C_ϕ and C_ψ terms of Eqs. (13) and (14) are no longer unphysical and must be retained in order that the normal components of the stress at this new surface can be fixed to zero.

With the two new boundary condition equations and the two new unknown potential constants, Eq. (16) becomes an 8×8 matrix equation. Using the Duhamel-Neumann expression for the stress [Eq. (15)], and assuming as before that there is no heating of the silicon, it can be shown that the new matrix equation takes the form

$$\mathbf{C}^f \mathbf{D}^f = \mathbf{F}^f, \quad (\text{A1})$$

where

$$\mathbf{C}^f = \begin{pmatrix} (1+p^2)e^{-nkh} & (1+p^2)e^{nkh} & 2ipe^{-pkh} & -2ipe^{pkh} & 0 & 0 & 0 & 0 \\ 2ine^{-nkh} & -2ine^{nkh} & -(1+p^2)e^{-nkh} & -(1+p^2)e^{nkh} & 0 & 0 & 0 & 0 \\ 1+p^2 & 1+p^2 & 2ip & -2ip & -(1+r^2)g & 2irg & -(1+r^2)g & -2irg \\ 2in & -2in & -(1+p^2) & -(1+p^2) & 2img & (1+r^2)g & -2img & (1+r^2)g \\ -1 & -1 & -ip & ip & 1 & -ir & 1 & ir \\ in & -in & -1 & -1 & im & 1 & -im & 1 \\ 0 & 0 & 0 & 0 & -g(1+r^2)e^{-mkH} & 2igre^{-rkH} & -g(1+r^2)e^{mkH} & -2igre^{-rkH} \\ 0 & 0 & 0 & 0 & 2igme^{-mkH} & g(1+r^2)e^{-rkH} & -2igme^{mkH} & g(1+r^2)e^{rkH} \end{pmatrix}, \quad (\text{A2})$$

$$\mathbf{D}^f = \begin{pmatrix} A_\phi \\ B_\phi \\ A_\psi \\ B_\psi \\ D_\phi \\ D_\psi \\ C_\phi \\ C_\psi \end{pmatrix}, \quad (\text{A3})$$

$$\mathbf{F}^f = \frac{iA\gamma}{v_{Tf}^2 p k v} \begin{pmatrix} \frac{-[\delta(k)+\delta(k-q)]}{k^2} + \frac{v_{Lf}^2}{k^2} \left(\frac{-(v_{Lf}^2 - 2v_{Tf}^2)}{v_{Lf}^2} + \frac{\xi^2}{k^2} \right) \left(\frac{\delta(k)}{v^2 + (v_{Lf}^2 \xi^2/k^2)} + \frac{\delta(k-q)}{v^2 + v_{Lf}^2 [(\xi^2 - k^2)/k^2]} \right) \\ \frac{2\xi v_{Tf}^2}{ik^3} \left(\frac{\delta(k)}{v^2 + (v_{Lf}^2 \xi^2/k^2)} + \frac{\delta(k-q)}{v^2 + v_{Lf}^2 [(\xi^2 - k^2)/k^2]} \right) \\ -\frac{e^{-\xi d} [\delta(k)+\delta(k-q)]}{k^2} + \frac{e^{-\xi d} v_{Lf}^2}{k^2} \left(\frac{-(v_{Lf}^2 - 2v_{Tf}^2)}{v_{Lf}^2} + \frac{\xi^2}{k^2} \right) \left(\frac{\delta(k)}{v^2 + (v_{Lf}^2 \xi^2/k^2)} + \frac{\delta(k-q)}{v^2 + v_{Lf}^2 [(\xi^2 - k^2)/k^2]} \right) \\ \frac{2e^{-\xi d} \xi v_{Tf}^2}{ik^3} \left(\frac{\delta(k)}{v^2 + (v_{Lf}^2 \xi^2/k^2)} + \frac{\delta(k-q)}{v^2 + v_{Lf}^2 [(\xi^2 - k^2)/k^2]} \right) \\ -\frac{e^{-\xi d} v_{Tf}^2}{k^2} \left(\frac{\delta(k)}{v^2 + (v_{Lf}^2 \xi^2/k^2)} + \frac{\delta(k-q)}{v^2 + v_{Lf}^2 [(\xi^2 - k^2)/k^2]} \right) \\ \frac{e^{-\xi d} \xi v_{Tf}^2}{k^3} \left(\frac{\delta(k)}{v^2 + (v_{Lf}^2 \xi^2/k^2)} + \frac{\delta(k-q)}{v^2 + v_{Lf}^2 [(\xi^2 - k^2)/k^2]} \right) \\ 0 \\ 0 \end{pmatrix}. \quad (\text{A4})$$

Information is extracted from this matrix equation with the same techniques that were used for the 6×6 equation in the main text. The resulting dispersion curves for the 30 lowest-velocity modes of a system composed of a 3 μm polyimide film on a 330 μm silicon substrate are shown in Fig. 13. One can see that relaxing the semi-infinite substrate assumption gives rise to extra plate modes propagating predominantly within the substrate with velocities above the substrate transverse velocity v_{Ts} which was, in the semi-infinite case, the cutoff for propagating modes of

the system. The dispersion curves for velocities sufficiently below the v_{Ts} are almost identical to those for the pseudo-Rayleigh modes calculated using the semi-infinite substrate system and shown in Fig. 12. The only differences occur at phase velocities near the cutoff and, for the lowest-velocity mode, at very low (< 0.2) qh values. This behavior is expected¹¹ and confirms that the semi-infinite substrate approximation is adequate to explain nearly all of the pseudo-Rayleigh modes seen in these experiments.

The extra plate modes above v_{Ts} are produced as a

result of acoustic reflections from the free substrate surface. They can be obtained within the semi-infinite substrate approximation as well, but only as "leaky" modes with finite lifetime due to energy flow into the infinite substrate.¹⁸ As eluded to in the main text, the existence of these modes for the polyimide/silicon system used in these experiments provides an explanation for the ISTS data points occurring above v_{Tf} in Fig. 12.

- ¹H. J. Eichler, P. Gunter, and D. W. Pohl, *Laser-Induced Dynamic Gratings* (Springer, Berlin, 1986).
- ²K. A. Nelson and M. D. Fayer, *J. Chem. Phys.* **72**, 5202 (1980); K. A. Nelson, D. R. Lutz, M. D. Fayer, and L. Madison, *Phys. Rev. B* **24**, 3261 (1981).
- ³A. R. Duggal and K. A. Nelson, *J. Chem. Phys.* **94**, 7677 (1991).
- ⁴J. S. Meth, C. D. Marshall, and M. D. Fayer, *J. Appl. Phys.* **67**, 3362 (1990).
- ⁵D. N. Rao, R. Burzynski, X. Mi, and P. N. Prasad, *Appl. Phys. Lett.* **48**, 388 (1986).
- ⁶A. R. Duggal, J. A. Rogers, K. A. Nelson, and M. Rothschild, *Appl. Phys. Lett.* **60**, 692 (1992).
- ⁷F. Nizzoli and J. R. Sandercock, in *Dynamical Properties of Solids*, edited by G. K. Horton and A. A. Maradudin (North-Holland, Amsterdam, 1990), Vol. 6, p. 283.
- ⁸Unpublished results.
- ⁹C. D. Marshall, I. M. Fishman, and M. D. Fayer, *Phys. Rev. B* **43**, 2696 (1991).
- ¹⁰Y. Yan Ph.D. thesis, Massachusetts Institute of Technology, 1988.
- ¹¹G. W. Farnell and E. L. Adler, in *Physical Acoustics, Principles and Methods*, edited by W. P. Mason and R. N. Thurston (Academic, New York, 1972), Vol. 9, p. 35.
- ¹²R. M. White, in *Methods of Experimental Physics*, edited by P. D. Edmonds (Academic, New York, 1981), Vol. 19, p. 495.
- ¹³V. Bortolani, A. M. Marvin, F. Nizzoli, and G. Santoro, *J. Phys. C* **16**, 1757 (1983).
- ¹⁴L. N. Durvasula and R. W. Gammon, *J. Appl. Phys.* **50**, 4339 (1979).
- ¹⁵E. V. Thompson, in *Encyclopedia of Polymer Science and Engineering*, edited by H. F. Mark, N. M. Bikales, C. G. Overberger, G. Menges, and J. I. Kroschwitz (Wiley, New York, 1985), Vol. 16, p. 711.
- ¹⁶B. Hartmann, in *Encyclopedia of Polymer Science and Engineering*, edited by H. F. Mark, N. M. Bikales, C. G. Overberger, G. Menges, and J. I. Kroschwitz (Wiley, New York, 1985), Vol. 1, p. 131.
- ¹⁷W. Nowacki, *Thermoelasticity* (Pergamon, New York, 1986).
- ¹⁸N. E. Glass and A. A. Marududin, *J. Appl. Phys.* **54**, 796 (1983).
- ¹⁹E. G. Lean, in *Progress in Optics*, edited by E. Wolf (North-Holland, Amsterdam, 1973), Vol. 11, p. 123.
- ²⁰R. C. Weast, M. J. Astle, and W. H. Beyer, Eds., *CRS Handbook of Chemistry and Physics*, 64th ed. (CRC, Boca Raton, FL, 1983).
- ²¹O. L. Anderson, in *Physical Acoustics, Principles and Methods*, edited by P. Mason and R. N. Thurston (Academic, New York, 1965), Vol. 3B, p. 77.
- ²²Technical Data Sheet, Dupont Co., Semiconductor Materials, Wilmington, DE.
- ²³G. Elsner, J. Kempf, J. W. Bartha, and H. H. Wagner, *Thin Solid Films* **185**, 189 (1990).
- ²⁴R. H. Lacombe and J. Greenblatt, in *Polyimides*, edited by K. L. Mittal (Plenum, New York, 1984), Vol. 2, p. 647.
- ²⁵S. Herminghaus, D. Boese, D. Y. Yoon, and B. A. Smith, *Appl. Phys. Lett.* **59**, 1043 (1991).
- ²⁶B. J. Factor, T. P. Russell, and M. F. Toney, *Phys. Rev. Lett.* **66**, 1181 (1991).